

Tuning of Structure, Morphology and Magnetism in Postperovskite Oxide Solid Solutions

Shigeto Hirai,[†] Takeshi Sanehira,[‡] Norimasa Nishiyama,[‡] Tetsuo Irifune,[‡]
Stephan Klemme,[§] Geoffrey Bromiley,[†] and J. Paul Attfield^{*-1}

[†]Centre for Science at Extreme Conditions and School of Geosciences, University of Edinburgh, Mayfield Road, Edinburgh EH9 3JZ, U.K., [‡]Geodynamics Research Center, Ehime University, 2-5 Bunkyo-cho, Matsuyama, Ehime 790-8577, Japan, [§]Institut für Mineralogie, Corrensstrasse 24, Universität Münster, 48149 Münster, Germany, and ¹Centre for Science at Extreme Conditions and School of Chemistry, University of Edinburgh, Mayfield Road, Edinburgh EH9 3JZ, U.K. j.p.attfield@ed.ac.uk

Received September 15, 2010. Revised Manuscript Received November 25, 2010

High-quality polycrystalline samples of postperovskite type $\text{CaIr}_{1-x}\text{Pt}_x\text{O}_3$ solid solutions ($x = 0.3, 0.5, 0.7$) and $\text{CaIr}_{0.5}\text{Rh}_{0.5}\text{O}_3$ have been synthesized at a pressure of 15 GPa, and their structures and properties are compared with those of CaIrO_3 . Substantial [100] grain growth is observed in all samples, leading to pronounced texture even in powdered materials. Small changes in the lattice constants and octahedral distortions are observed across the $\text{CaIr}_{1-x}\text{Pt}_x\text{O}_3$ series. CaIrO_3 is semiconducting and shows temperature-independent paramagnetism and an ordered moment of $0.04 \mu_B$ below a 108 K magnetic transition. Doping with Pt or Rh induces Curie–Weiss paramagnetism and suppresses the magnetic transition to zero for $\sim 40\%$ Pt doping. The anisotropic structure and morphology of CaIrO_3 combined with the Ir^{4+} spin–orbit coupling results in a large magnetic anisotropy constant of $1.77 \times 10^6 \text{ J m}^{-3}$, comparable to values for permanent magnet materials.

I. Introduction

Since the discovery of the perovskite to postperovskite transition in MgSiO_3 in a laser-heated diamond anvil cell,¹ wide attention has been focused on the postperovskite phase of MgSiO_3 . This is because the postperovskite phase is likely to play a key role in processes occurring in Earth's lower mantle, and the perovskite to postperovskite transition can explain many features of the D'' seismic discontinuity there. Although it is important to conduct further studies on MgSiO_3 , this postperovskite phase has not been quenched to ambient conditions; this is also the case for the postperovskite type transition metal oxides Fe_2O_3 ² and Mn_2O_3 .³ Thus, it is useful to investigate the materials properties of structural analogues of the MgSiO_3 postperovskite that are quenchable. The electronic and magnetic properties of transition metal analogues are also of interest because postperovskite type oxides are rare, and their physical properties have not been extensively explored.

The postperovskite phase of MgSiO_3 adopts the layered CaIrO_3 -type structure containing corner-linked chains of edge-sharing octahedra (Figure 1). Four quenchable CaIrO_3 -type oxides have been reported to date:

CaIrO_3 ,⁴ CaPtO_3 ,⁵ CaRhO_3 ,⁶ and CaRuO_3 .⁷ Polycrystalline CaIrO_3 can be synthesized at ambient pressure from binary oxides heated to 1273 K in an evacuated silica tube, and single crystals of CaIrO_3 were synthesized at 1223 K using a CaCl_2 flux.⁴ The other three oxides were obtained using a multianvil apparatus to achieve high pressure (P) and temperature (T) conditions: CaPtO_3 (4 GPa, 1073 K),⁵ CaRhO_3 (6 GPa, 1473 K),⁶ and CaRuO_3 (23 GPa, 1223 K).⁷ Further studies on these materials have revealed postperovskite-to-perovskite structural phase transitions at high P–T. The postperovskite phase of CaIrO_3 transforms to the perovskite structure at 2 GPa, 1673 K,⁸ and this transformation was also observed for CaRhO_3 (6 GPa, 1873 K) and CaRuO_3 (23 GPa, 1343 K), whereas CaPtO_3 remained in the postperovskite structure at higher temperatures.⁹ The former observations show that the perovskite type is the high-temperature phase for these CaMO_3 postperovskites, and this was supported by a Raman spectroscopy study of CaIrO_3 up to 30 GPa¹⁰ and a synchrotron X-ray diffraction of CaPtO_3 up to

- (1) Murakami, M.; Hirose, K.; Kawamura, K.; Sata, K.; Ohishi, Y. *Science* **2004**, *304*, 855–858.
- (2) Shim, S.; Bengtson, A.; Morgan, D.; Sturhahn, W.; Catalli, K.; Zhao, J.; Lerche, M.; Prakapenka, V. B. *Proc. Natl. Acad. Sci. U.S.A.* **2009**, *106*, 5508–5512.
- (3) Santillan, J.; Shim, S.; Shen, G.; Prakapenka, V. B. *Geophys. Res. Lett.* **2006**, *33*, L15307.
- (4) Hirai, S.; Welch, M. D.; Aguado, F.; Redfern, S. A. T. *Z. Kristallogr.* **2009**, *224*, 345–350.

- (5) Ohgushi, K.; Matsushita, Y.; Miyajima, N.; Katsuya, Y.; Tanaka, M.; Izumi, F.; Gotou, H.; Ueda, Y.; Yagi, T. *Phys. Chem. Miner.* **2008**, *35*, 189–195.
- (6) Yamaura, K.; Shirako, Y.; Kojitani, H.; Arai, M.; Young, D. P.; Akaogi, M.; Nakashima, M.; Katsumata, T.; Inaguma, Y.; Takayama-Muromachi, E. *J. Am. Chem. Soc.* **2009**, *131*, 2722–2726.
- (7) Kojitani, H.; Shirako, Y.; Akaogi, M. *Phys. Earth. Planet. Inter.* **2007**, *165*, 127–134.
- (8) Kojitani, H.; Furukawa, A.; Akaogi, M. *Am. Mineral.* **2007**, *92*, 229–232.
- (9) Inaguma, Y.; Hasumi, K.; Yoshida, M.; Ohba, T.; Katsumata, T. *Inorg. Chem.* **2008**, *47*, 1868–1870.
- (10) Hustoft, J.; Shim, S.; Kubo, A.; Nishiyama, N. *Am. Mineral.* **2008**, *93*, 1654–1658.

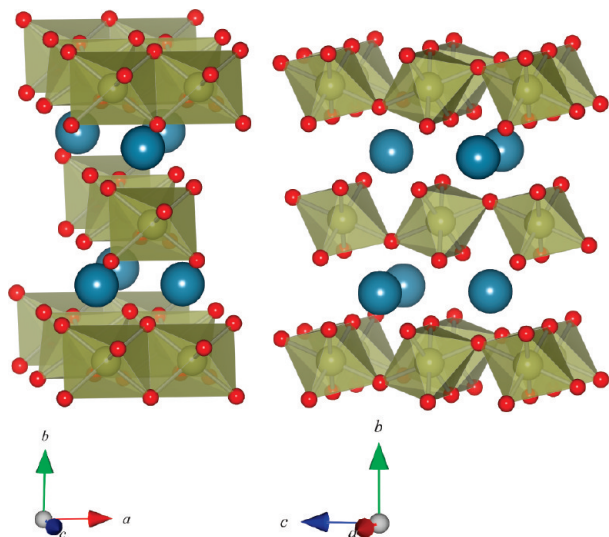


Figure 1. Crystal structure of postperovskite type CaIrO_3 showing layers of edge- and corner-sharing IrO_6 octahedra, separated by Ca ions.

40 GPa,¹¹ which show that the phase transition from postperovskite to perovskite transition does not occur at room temperature.

The presence of transition metal ions in the above CaMO_3 postperovskites suggests that such phases might have interesting electronic or magnetic properties. A study of $\text{Ca}_{1-x}\text{Na}_x\text{IrO}_3$ solid solutions (synthesized at 4 GPa, 1073 K)¹² revealed a metal–insulator transition at $x = 0.37$. To investigate such properties further, we have explored the $\text{CaIr}_{1-x}\text{Pt}_x\text{O}_3$ series, and the synthesis and structural and physical properties of these solid solutions are reported here. We also demonstrate that $\text{CaIr}_{1-x}\text{Rh}_x\text{O}_3$ materials are accessible, as we report the $x = 0.5$ member of this series.

II. Experimental Section

Polycrystalline samples of CaIrO_3 postperovskite were synthesized by solid state reaction from CaO and IrO_2 . CaO powder was prepared from CaCO_3 by heating in air at 1000 °C for 24 h. Well-ground mixtures of the starting materials in the stoichiometric ratio were sealed in an evacuated silica tube and heated in air at 1273 K over 20 h. CaIrO_3 postperovskite single crystals were synthesized by a flux method.⁴

Polycrystalline samples of $\text{CaIr}_{1-x}\text{Pt}_x\text{O}_3$ and $\text{CaIr}_{0.5}\text{Rh}_{0.5}\text{O}_3$ were synthesized at high pressure–temperature conditions. $\text{CaIr}_{1-x}\text{Pt}_x\text{O}_3$ ($x = 0.3, 0.5, 0.7$) was synthesized by solid-state reaction from CaO , IrO_2 , and PtO_2 powders. Well-ground mixtures of the starting materials in the appropriate molar ratios were placed into a Au capsule ($\phi = 2.5$ mm) sandwiched by BN composite disks ($\phi = 2.7$ mm). $\text{CaIr}_{0.5}\text{Rh}_{0.5}\text{O}_3$ was synthesized by solid-state reaction from CaO , IrO_2 , and Rh_2O_3 , with KClO_4 as an oxidizer. A well-ground mixture of the starting materials in a ratio of 1/0.5/0.5/4.07 (Ca/Ir/Rh/O) was placed into a Au capsule ($\phi = 2.5$ mm) sandwiched by MgO disks ($\phi = 2.7$ mm) to avoid sample reduction. The capsules were heated in a multianvil apparatus at 1573 K and 15 GPa

pressure for 40 min, followed by rapid quenching to ambient temperature, and then release of pressure. A pressure of 15 GPa was used to ensure that homogeneous solid solutions were formed because reactions at 3 and 10 GPa gave samples with a range of Ir/Pt ratios and containing IrO_2 and Pt secondary phases. Dense black pellets were obtained, and that of $\text{CaIr}_{0.5}\text{Rh}_{0.5}\text{O}_3$ was washed with distilled water to remove KCl.

Powdered samples were investigated by powder X-ray diffraction (XRD) using a Bruker D8 diffractometer in reflection geometry with monochromated Cu $\text{K}\alpha 1$ radiation. Two patterns were collected for each sample: one from the loosely packed powder, and the other from the powder sieved onto a sample holder covered by a thin layer of organic grease to minimize preferred orientation of crystallites. The GSAS software was used for Rietveld refinement of the crystal structure and texture analysis.¹³ Raman spectra on $\text{CaIr}_{1-x}\text{Pt}_x\text{O}_3$ ($x = 0.3, 0.5, 0.7$) and $\text{CaIr}_{0.5}\text{Rh}_{0.5}\text{O}_3$ were collected using a Jobin Yvon LabRAM instrument ($\lambda = 632.8$ nm). Scanning electron microscopy with energy-dispersive X-ray analysis (SEM/EDX) was conducted on a polished surface of selected samples using a Phillips XL30CP, with PGT Spirit X-ray analysis, using an acceleration voltage of 20 kV.

Electrical resistivities of rectangular pellets were studied by a four-point probe method with a gauge current of 0.99 mA. Electrical contacts were made from Cu wires and silver paste. Magnetizations were measured using a Quantum Design MPMS SQUID magnetometer. Zero-field and field-cooled (ZFC and FC) measurements were made with a field of 100 Oe after cooling the sample to 5 K.

III. Results

A. Structure and Morphology. XRD patterns (Figure 2) demonstrate that the recovered $\text{CaIr}_{1-x}\text{Pt}_x\text{O}_3$ ($x = 0, 0.3, 0.5, 0.7$) and $\text{CaIr}_{0.5}\text{Rh}_{0.5}\text{O}_3$ samples contain postperovskites with traces of secondary phases in some cases. All of the major XRD peaks are indexed by the CaIrO_3 -type cell with orthorhombic space group $Cmcm$. The Raman spectra are similar to that for CaIrO_3 , and the shifts of the five primary Raman modes of $\text{CaIr}_{1-x}\text{Pt}_x\text{O}_3$ series (Table 1) confirm that solid solutions are present. The ν_4 Raman mode is not observed in CaIrO_3 but appears near 563 cm^{-1} for all the Pt or Rh doped samples.

The morphologies and stoichiometries of the samples were examined by SEM/EDX analysis for $\text{CaIr}_{0.5}\text{Rh}_{0.5}\text{O}_3$ and by using an electron microprobe for $\text{CaIr}_{1-x}\text{Pt}_x\text{O}_3$ ($x = 0, 0.3, 0.5, 0.7$). Traces of additional elements were not detected for any of the samples by EDX, and the stoichiometries were confirmed as being the same as the nominal compositions. The crystallites show a needlelike morphology in all samples. The growth of needlelike grains elongated in the a -axis direction was previously reported for CaIrO_3 and CaPtO_3 .^{2,3,14} The mean grain size varies in the range 1–8 μm between samples, as shown in the micrographs in Figure 3 and as summarized in Table 2. Large grains are also observed for polycrystalline CaIrO_3 postperovskite, prepared at ambient pressures and temperatures around 1273 K. For the

(11) Lindsay-Scott, A.; Wood, I. G.; Dobson D. P.; Vocadlo, L.; Brodholt, J. P.; Crichton, W.; Hanfland, M.; Taniguchi, T. *Phys. Earth Planet. Inter.* **2010**, *182*, 113–118.

(12) Ohgushi, K.; Gotou, H.; Yagi, T.; Kiuchi, Y.; Sakai, F.; Ueda, Y. *Phys. Rev. B* **2006**, *74*, 241104.

(13) Larson, A. C.; Von Dreele, R. B. *Los Alamos National Laboratory Report LAUR* **2000**, 86–748.

(14) Miyajima, N.; Ohgushi, K.; Ichihara, M.; Yagi, T. *Geophys. Res. Lett.* **2006**, *33*, L12302.

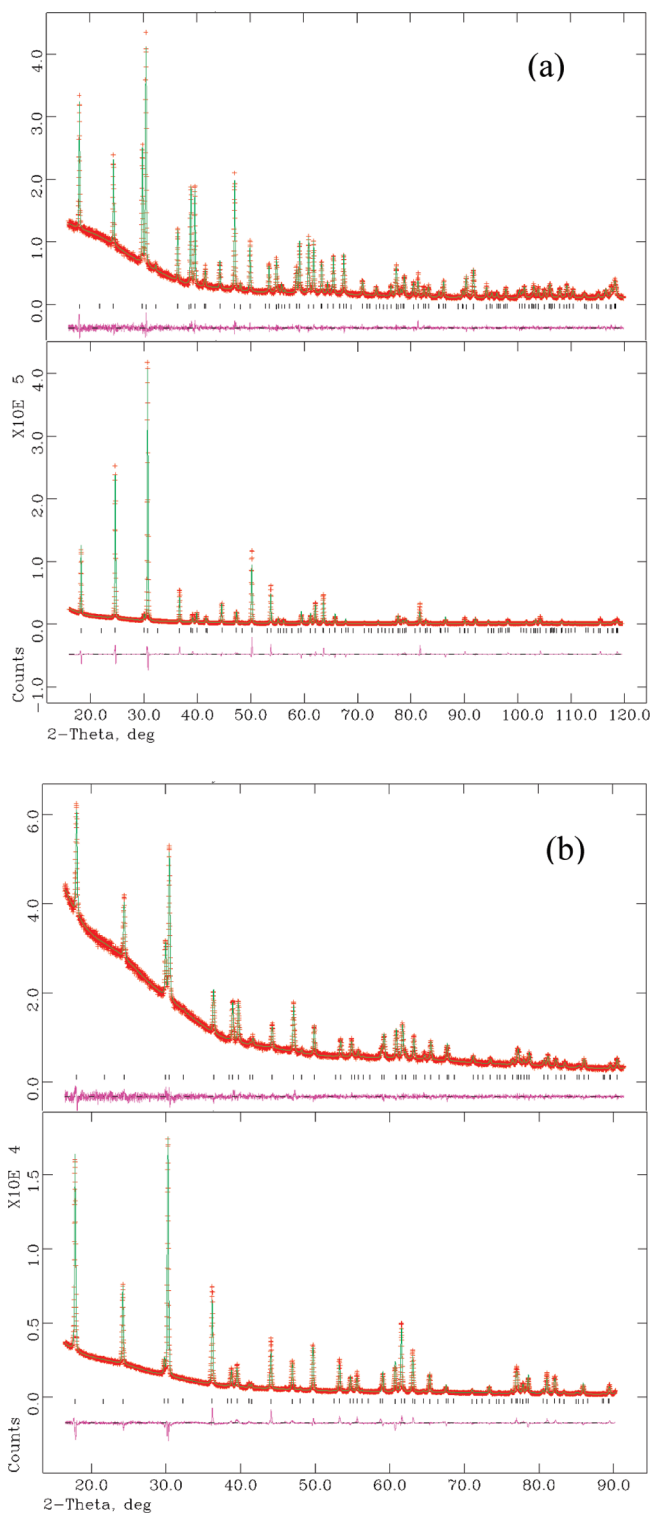


Figure 2. Fitted powder X-ray diffraction profiles of (a) CaIrO_3 and (b) $\text{CaIr}_{0.5}\text{Pt}_{0.5}\text{O}_3$ (upper/lower panels are for powdered samples on greased/ungreased holders, showing considerable texture effects in the latter).

$\text{CaIr}_{1-x}\text{Pt}_x\text{O}_3$ samples prepared at 15 GPa and 1573 K, grain growth is greater for $x = 0.5$ than for $x = 0.3$ and 0.7 , suggesting that the melting point does not vary monotonically in the $\text{CaIr}_{1-x}\text{Pt}_x\text{O}_3$ series and, instead, has a minimum near $x = 0.5$.

Initial Rietveld fits to the XRD profiles showed that strong textures were present in the loosely packed powders, so another pattern was collected from each sample

sieved onto a greased surface to minimize this effect. Large differences between the two patterns for each sample are evident in Figure 2. Fits for the greased samples were used to refine the crystal structure parameters, giving the results shown in Table 2. The variation of lattice parameters with composition in the $\text{CaIr}_{1-x}\text{Pt}_x\text{O}_3$ series is shown in Figure 4, taking results for CaPtO_3 from ref 5. It is notable that the a - and b -axis lengths change linearly with composition, whereas the c -axis shows curvature and lies below the values expected by linear interpolation between the end-members for $0 < x < 1$. This leads to the same trend in the cell volume. This nonlinearity (and, hence, a deviation from Vegard's law) suggests that some local ordering or clustering of Ir/Pt occurs within the chains of corner-sharing octahedra along the c -direction of the crystal structure (Figure 1). This local order is consistent with the apparent minimum in the melting point near $x = 0.5$ noted above.

The Ir/Pt/RhO₆ octahedra show a tetragonal compression in the $\text{CaIr}_{1-x}\text{Pt}_x\text{O}_3$ structures and in $\text{CaIr}_{0.5}\text{Rh}_{0.5}\text{O}_3$, with two short M–O1 (1.91–1.99 Å) and four long M–O2 (2.04–2.09 Å) bonds (Table 2). No systematic changes in the O–M–O angles or M–O–M angles are evident. The octahedral distortion is consistent with the connectivity of the postperovskite structure. Applying the bond valence principle¹⁵ that the summed valences of the bonds around a cation or anion should equal the formal valence gives theoretical M–O1 and M–O2 valences of 12/17 (≈ 0.71) and 11/17 (≈ 0.65), respectively, showing that the M–O1 bonds are expected to be slightly stronger and shorter than the M–O2. These values compare well to experimental bond valences in Table 2 calculated from the standard function $\exp((d_i - d_0)/B)$ and parameters, where d_i is the bond distance, d_0 is a constant for a particular atom pair, and $B = 0.37$ Å. Appropriate averages of d_0 constants were used for Ir/Pt and Ir/Rh solid solutions, and the M site bond valence sums (BVSs) are close to the expected +4 value. The anisotropy of the structure also results in strained CaO₈ polyhedra, with BVSs between 2.1 and 2.4.

An electronic influence on the octahedral distortions is also evident from the octahedral distortion parameter $\Delta d = 1/6\{2(d_1 - d)^2 + 4(d_2 - d)^2\}/d^2$ (d_1 : M–O1 bond distance, d_2 : M–O2 bond distance, d : average M–O distance).¹⁶ Figure 4e shows that Δd decreases across the $\text{CaIr}_{1-x}\text{Pt}_x\text{O}_3$ series as the triply degenerate ground state of low-spin $5d^5$ Ir⁴⁺ is replaced by nondegenerate $5d^6$ Pt⁴⁺. The tetragonal compression of the octahedra is not consistent with a Jahn–Teller distortion of low-spin $5d^5$ Ir⁴⁺ because tetragonal elongation is needed to break the electronic degeneracy of the t_{2g}^5 configuration and probably reflects a strong spin–orbit coupling effect in Ir⁴⁺.

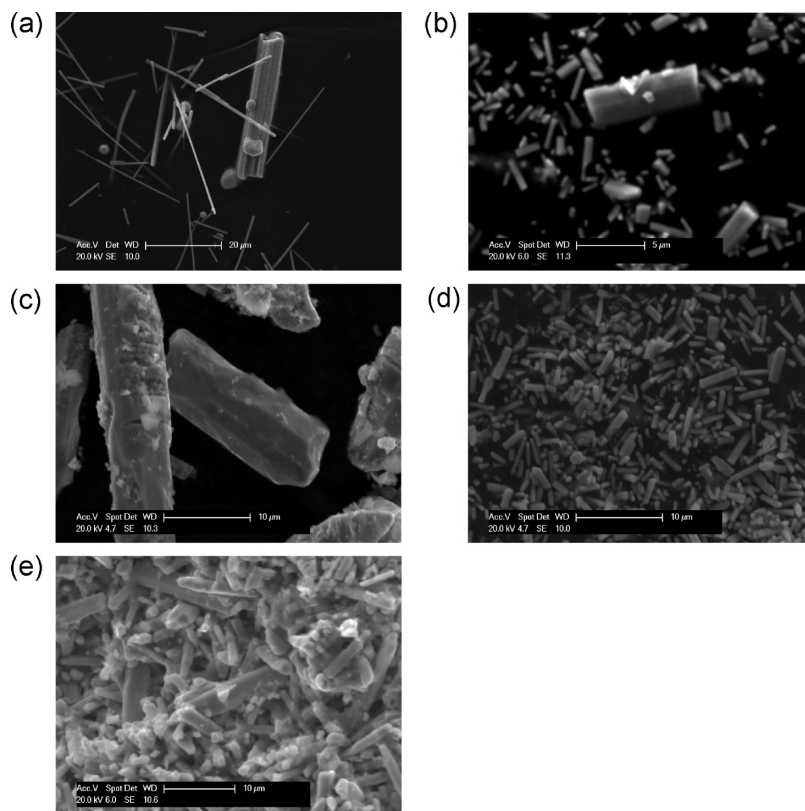
To obtain morphological information from the XRD patterns of loosely packed powders, the crystal structure parameters were fixed at the values obtained from the

(15) Brown, I. D. *The Chemical Bond in Inorganic Chemistry*; Oxford University Press: Oxford, 2002.

(16) Alonso, J. A.; Martinez-Lopez, M. J.; Casais, M. T. *Inorg. Chem.* **2000**, *39*, 917–923.

Table 1. Frequencies of the Five Primary Raman Modes of $\text{CaIr}_{1-x}\text{Pt}_x\text{O}_3$ and $\text{CaIr}_{0.5}\text{Rh}_{0.5}\text{O}_3$

frequency (cm^{-1})	CaIrO_3	$\text{CaIr}_{0.7}\text{Pt}_{0.3}\text{O}_3$	$\text{CaIr}_{0.5}\text{Pt}_{0.5}\text{O}_3$	$\text{CaIr}_{0.3}\text{Pt}_{0.7}\text{O}_3$	$\text{CaIr}_{0.5}\text{Rh}_{0.5}\text{O}_3$
ν_1	309	322	320	334	301
ν_2	444	452	451	452	449
ν_3	552	543	544	553	546
ν_4		562	559	568	565
ν_5	712	688	692	703	648

**Figure 3.** Typical SEM image of grains of $\text{CaIr}_{1-x}\text{Pt}_x\text{O}_3$ for (a) $x=0$ (scale bar = 20 μm), (b) $x=0.3$ (5 μm), (c) $x=0.5$ (10 μm), (d) $x=0.7$ (10 μm), and (e) $\text{CaIr}_{0.5}\text{Rh}_{0.5}\text{O}_3$ (10 μm).

greased samples, and the intensities were Rietveld-fitted by varying the six ODF (orientation density function) coefficients that describe a cylindrical symmetry sample texture up to fourth order.¹⁷ This gave a good fit to the peak intensities, as shown in Figure 2.

The orientation densities derived from the refined ODF parameters are shown in Figure 5. These show the density of crystallites with plane (hkl) at an angle ψ to the sample plane, relative to the average (untextured) value of 1.0. In all samples, the maximum density for (100) is at $\psi = 90^\circ$, confirming that the crystallographic a -axis is parallel to the long dimension of the needlelike crystals. Both the (010) and (001) densities are consequently peaked at $\psi = 0$, but a systematic change from (001) to (010) density is observed as x increases from $x=0$ to 0.7. This shows that Pt substitution favors (001) over (010) growth. The magnitudes of the orientation density maxima in the $\text{CaIr}_{1-x}\text{Pt}_x\text{O}_3$ series correlate well with the grain sizes observed by SEM. The large-grain CaIrO_3 and $\text{CaIr}_{0.5}\text{Pt}_{0.5}\text{O}_3$ show maximum densities of near 3, whereas the

smaller-grained $\text{CaIr}_{0.7}\text{Pt}_{0.3}\text{O}_3$ and $\text{CaIr}_{0.3}\text{Pt}_{0.7}\text{O}_3$ have density maxima of 1.4 and 2.1, respectively. However, the $\text{CaIr}_{0.5}\text{Rh}_{0.5}\text{O}_3$ sample shows the most extreme texture, with an (001) density of 4.0 at $\psi = 0$.

B. Electronic and Magnetic Properties. The temperature dependences of electrical resistivity for CaIrO_3 , $\text{CaIr}_{0.5}\text{Pt}_{0.5}\text{O}_3$, and $\text{CaIr}_{0.5}\text{Rh}_{0.5}\text{O}_3$ are shown in Figure 6. The samples are narrow-bandgap semiconductors with bandgap energies of 34–150 meV (Table 3) estimated from the 290 K gradient of Arrhenius plots.

Figure 7 shows the temperature dependence of magnetic susceptibility for the five samples. A ferromagnetic transition, marked by an upturn in magnetization and divergence of zero-field and field-cooled susceptibilities is observed for CaIrO_3 at $T_C = 108$ K, which is comparable to a previously reported value.¹² Transitions are seen at the same temperature for all the $\text{CaIr}_{1-x}\text{Pt}_x\text{O}_3$ solid solutions, showing that traces of CaIrO_3 are present, although these were not observed in the EDX analyses. The intrinsic transition is suppressed to 20 K for $x = 0.3$ and is not observed down to 5 K for the $x = 0.5$ and 0.7 samples. $\text{CaIr}_{0.5}\text{Rh}_{0.5}\text{O}_3$ shows the ferromagnetic

Table 2. Average Grain Sizes and Crystallographic Results^a for CaIr_{1-x}Pt_xO₃ and CaIr_{0.5}Rh_{0.5}O₃

	compounds				
	CaIrO ₃	CaIr _{0.7} Pt _{0.3} O ₃	CaIr _{0.5} Pt _{0.5} O ₃	CaIr _{0.3} Pt _{0.7} O ₃	CaIr _{0.5} Rh _{0.5} O ₃
grain size (μm)	8.0	1.0	8.0	2.0	3.0
<i>a</i> (Å)	3.14592(4)	3.14114(7)	3.13575(7)	3.13216(4)	3.11997(6)
<i>b</i> (Å)	9.8635(1)	9.8795(2)	9.8924(1)	9.9051(1)	9.8652(1)
<i>c</i> (Å)	7.29903(9)	7.3081(1)	7.3169(1)	7.3303(1)	7.2930(1)
<i>V</i> (Å ³)	226.489(6)	226.795(12)	226.973(9)	227.420(7)	224.476(8)
<i>R</i> _{wp}	0.0560	0.0350	0.0359	0.0337	0.0634
χ ²	1.17	1.17	1.20	1.08	1.62
Ca: <i>y</i>	0.2503(3)	0.2474(6)	0.2510(5)	0.2500(4)	0.2484(4)
O1: <i>y</i>	0.425(1)	0.439(2)	0.429(2)	0.421(1)	0.441(2)
O2: <i>y</i>	0.1320(8)	0.127(1)	0.128(1)	0.1291(8)	0.132(1)
O2: <i>z</i>	0.4455(9)	0.451(2)	0.449(1)	0.450(1)	0.435(1)
U _{iso} (Å ²)	0.0024(5)	0.0131(6)	0.0009(5)	0.0037(6)	0.0077(9)
M–O1 (Å)	1.967(5) × 2	1.923(5) × 2	1.957(7) × 2	1.993(5) × 2	1.913(5) × 2
M–O2 (Å)	2.081(5) × 4	2.041(7) × 4	2.053(7) × 4	2.055(6) × 4	2.087(7) × 4
⟨M–O⟩ (Å)	2.041(5)	1.999(6)	2.019(7)	2.032(6)	2.026(6)
M–O1 valence	0.77(1)	0.87(1)	0.80(2)	0.73(1)	0.87(1)
M–O2 valence	0.56(1)	0.63(1)	0.62(1)	0.62(1)	0.55(1)
BVS (Ir)	3.78(6)	4.26(6)	4.08(8)	3.94(6)	3.94(6)
M–O1–M (deg)	136.1(7)	143.7(9)	138(1)	133.7(7)	145(1)
M–O2–M (deg)	98.2(3)	100.6(5)	99.6(4)	99.3(4)	96.8(4)
O1–M–O2 (deg)	93.3(3)	91.3(4)	92.8(5)	94.5(3)	91.6(4)
O2–M–O2 (deg)	98.2(3)	100.6(5)	99.6(4)	99.3(4)	96.8(4)

^a Atomic positions; Ca: 4c (0, *y*, 1/4), M=Ir/Pt/Rh: 4a (0, 0, 0), O1: 4c (0, *y*, 1/4), O2: 8f (0, *y*, *z*); bond valences of M–O bonds were calculated as exp((*d*₀–*d*)/*B*) with *d*₀ values of 1.870 (Ir⁴⁺–O²⁻), 1.879 (Pt⁴⁺–O²⁻), 1.857 (Rh⁴⁺–O²⁻).

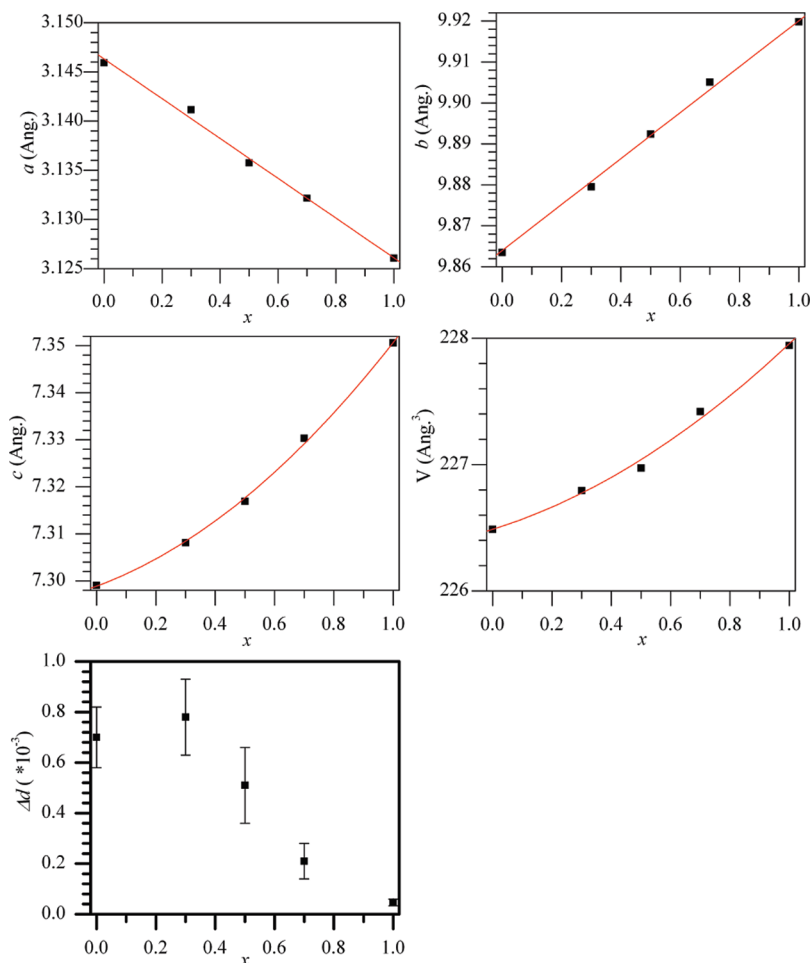


Figure 4. Evolution of the orthorhombic lattice parameters, unit cell volume (*V*) and octahedral distortion parameter Δd , as defined in the text, for CaIr_{1-x}Pt_xO₃ solid solutions. The fitted curves are guides to the eye. Data for CaPtO₃ are taken from ref 5.

transition at 40 K. Hence, both Pt and Rh substitutions suppress the magnetic transition in CaIrO₃ with a more

rapid suppression by diamagnetic Pt⁴⁺ than by magnetic Rh⁴⁺.

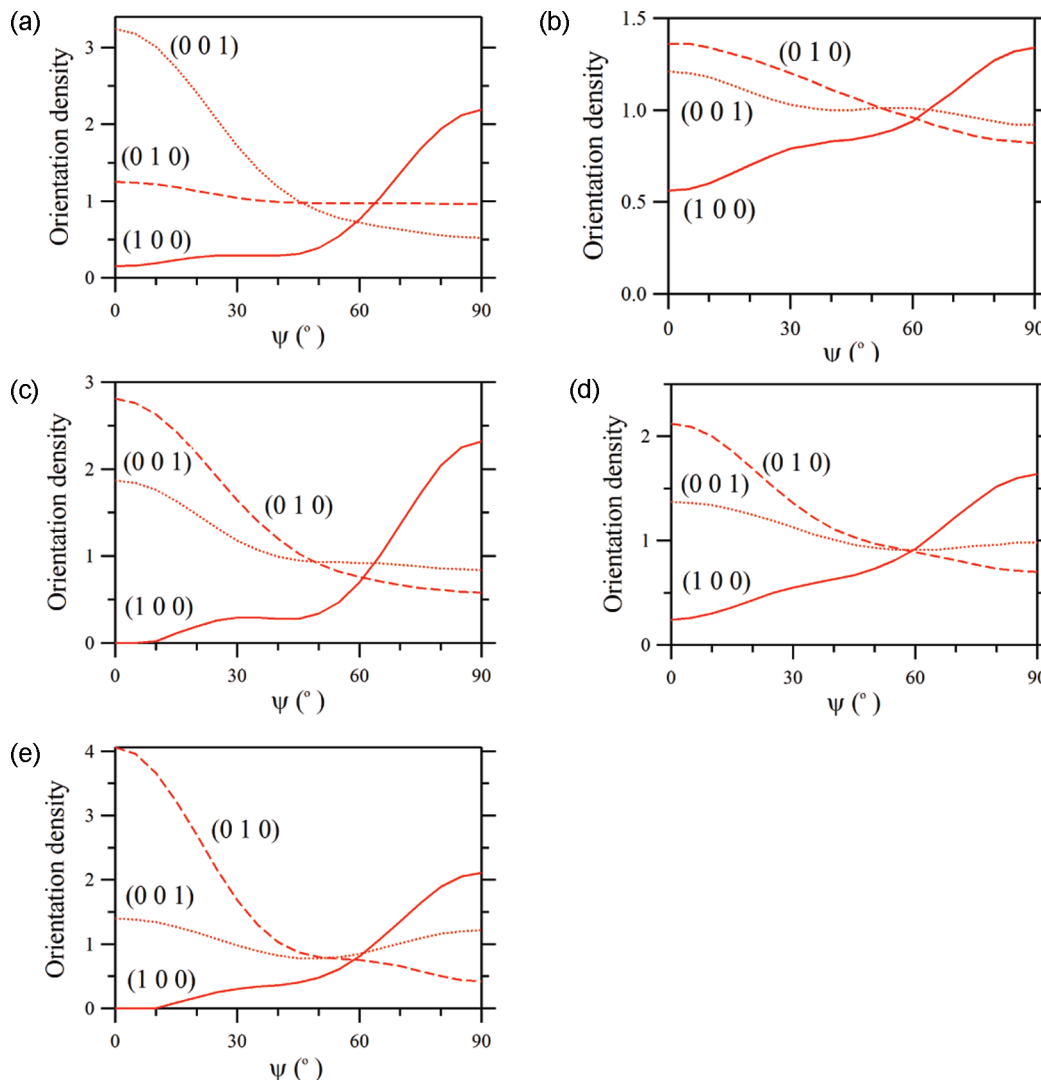


Figure 5. Angular dependence of crystallite orientation density of $\text{CaIr}_{1-x}\text{Pt}_x\text{O}_3$ for (a) $x=0$, (b) $x=0.3$, (c) $x=0.5$ (d) $x=0.7$, and of (e) $\text{CaIr}_{0.5}\text{Rh}_{0.5}\text{O}_3$.

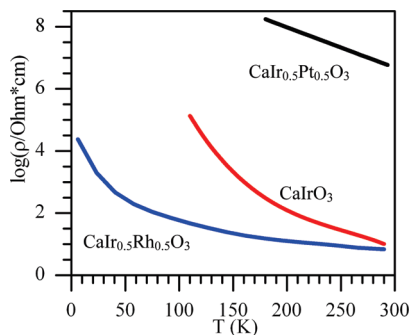


Figure 6. Temperature dependence of electrical resistivity for $\text{CaIr}_{0.5}\text{Rh}_{0.5}\text{O}_3$, CaIrO_3 and $\text{CaIr}_{0.5}\text{Pt}_{0.5}\text{O}_3$.

The 150–300 K inverse susceptibilities are shown in the insets to Figure 7. CaIrO_3 shows temperature-independent paramagnetism over this range, but the other samples have nonlinear susceptibilities. These were fitted using the equation $1/\chi = [\alpha + C/T - \theta]^{-1}$ which combines temperature-independent and Curie–Weiss terms. The fitted curves are shown in Figure 7, and the derived parameters are in Table 3. These show that CaIrO_3 appears to be close to a metal–insulator transition because it shows

only temperature-independent paramagnetic behavior at high temperatures, despite appearing nonmetallic. Doping with Pt suppresses the near-metallic behavior as the resistivity increases by 6 orders of magnitude for $x = 0.5$, decreases the temperature-independent paramagnetism, and gives rise to local moments, although Pt^{4+} is diamagnetic. These follow Curie–Weiss behavior with an effective paramagnetic moment of $\sim 0.5 \mu_B$ /formula unit, and the positive Weiss constants evidence ferromagnetic exchange interactions between spins. In contrast, $\text{CaIr}_{0.5}\text{Rh}_{0.5}\text{O}_3$ has a small, negative θ , although this is almost within error of zero.

Magnetization-field data for CaIrO_3 , $\text{CaIr}_{0.7}\text{Pt}_{0.3}\text{O}_3$, and $\text{CaIr}_{0.5}\text{Rh}_{0.5}\text{O}_3$ are shown in Figure 8. Ferromagnetic hysteresis loops are observed for the former two materials, but $\text{CaIr}_{0.5}\text{Rh}_{0.5}\text{O}_3$ appears to have only short-range ferromagnetic interactions. CaIrO_3 is an unusually hard magnetic oxide, with a large magnetic anisotropy and a coercive field of $H_c = 3.4$ T at 5 K for the present sample.

(18) Nunes, W. C.; Folly, W. S. D.; Sinnecker, J. P.; Novak, M. A. *Phys. Rev. B* **2004**, *70*, 014419.

(19) Blundell, S. *Magnetism in Condensed Matter*; Oxford University Press: Oxford, **2001**, pp 128–136.

Table 3. Electronic and Magnetic Parameters of $\text{CaIr}_{1-x}\text{Pt}_x\text{O}_3$ and $\text{CaIr}_{0.5}\text{Rh}_{0.5}\text{O}_3$

	compounds				
	CaIrO_3	$\text{CaIr}_{0.7}\text{Pt}_{0.3}\text{O}_3$	$\text{CaIr}_{0.5}\text{Pt}_{0.5}\text{O}_3$	$\text{CaIr}_{0.3}\text{Pt}_{0.7}\text{O}_3$	$\text{CaIr}_{0.5}\text{Rh}_{0.5}\text{O}_3$
E_g (eV)	0.14		0.15		0.034
$\rho_{290\text{K}}$ ($\Omega\text{ cm}$)	10.1		8.37×10^6		6.79
α (emu mol^{-1})	0.00748(1)	0.00024(2)	0.00126(1)	0.00043(1)	0.00043(1)
θ (K)		37(11)	87(7)	39(8)	-16(12)
C (emu K mol^{-1})		0.053(9)	0.02(1)	0.031(7)	0.028(9)
μ_{eff} ($\mu_B/\text{f.u.}$)		0.7(3)	0.4(3)	0.5(2)	0.5(3)
T_c (K)	108	20			40

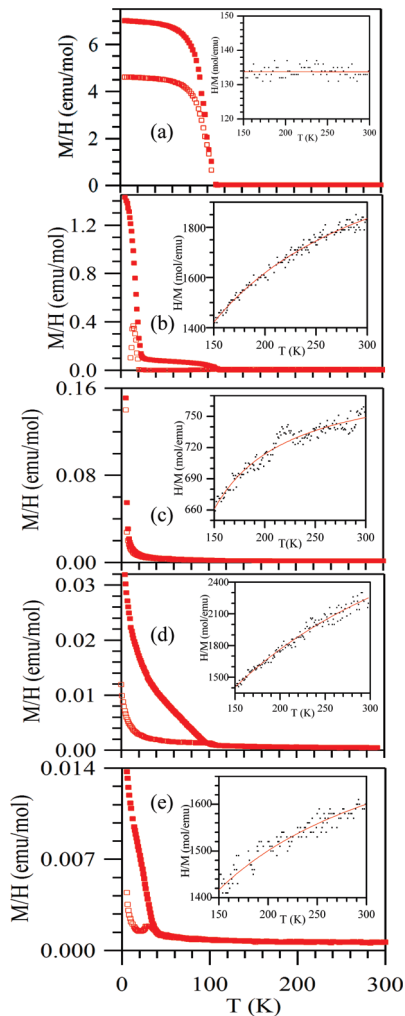


Figure 7. ZFC and FC (open and closed symbols) magnetic susceptibilities (M/H) of $\text{CaIr}_{1-x}\text{Pt}_x\text{O}_3$ for (a) $x=0$, (b) $x=0.3$, (c) $x=0.5$, (d) $x=0.7$, and of (e) $\text{CaIr}_{0.5}\text{Rh}_{0.5}\text{O}_3$. Insets show fits to inverse susceptibilities between 150 and 300 K.

The thermal evolution of the hysteresis loop is also shown in Figure 8a. The variation of the coercive field with temperature (Figure 9) was fitted with the equation¹⁸ $H_c = 2\alpha K/M_s[1 - (T/T_C)^{1/2}]$ where $\alpha = 0.48$, and the fitted uniaxial anisotropy constant is $K = 1.77 \times 10^6 \text{ J m}^{-3}$. This is comparable to the value of $5 \times 10^6 \text{ J m}^{-3}$ for $\text{Nd}_2\text{Fe}_{14}\text{B}$, which is a widely used permanent magnet material.^{19,20}

The large crystal field and the strong spin-orbit coupling of Ir^{4+} ($5d^5$), as found in a recent study on Sr_2IrO_4 ,²¹ and

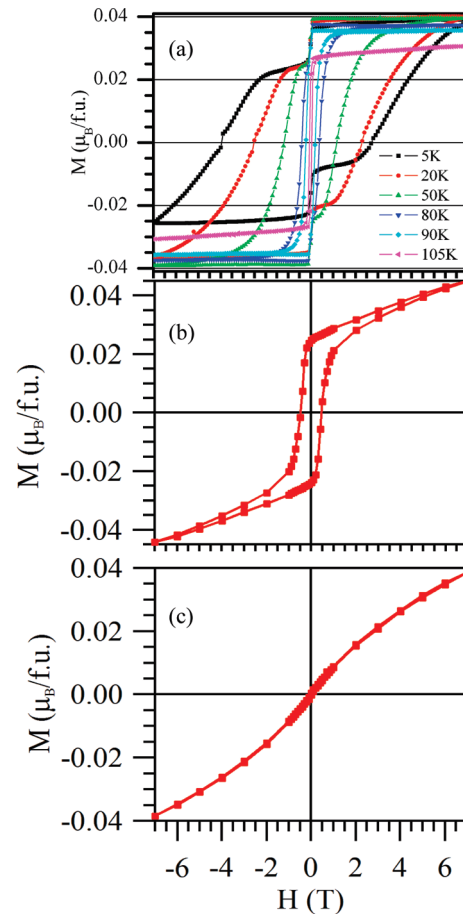


Figure 8. Magnetization-field hysteresis loops for (a) CaIrO_3 at temperatures between 5 and 105 K, (b) $\text{CaIr}_{0.7}\text{Pt}_{0.3}\text{O}_3$ at 5 K, and (c) $\text{CaIr}_{0.5}\text{Rh}_{0.5}\text{O}_3$ at 5 K.

the anisotropic crystal structure and morphology of CaIrO_3 are all likely contributors to this exceptionally high coercivity for a magnetic oxide. Substitution of 30% Pt for Ir dilutes the magnetic interactions and decreases the saturated magnetization from $0.040 \mu_B/\text{formula unit}$ for CaIrO_3 to $0.024 \mu_B/\text{formula unit}$ while the 5K coercive field drops to 0.46T.

IV. Discussion

To date, the only quenchable oxides having the post-perovskite (CaIrO_3) structure are CaMO_3 for $M = \text{Ru}$,

(20) Haskel, D.; Lang, J. C.; Islam, Z.; Cady, A.; Srajer, G.; Veenendaal, M.; Canfield, P. C. *Phys. Rev. Lett.* **2005**, *95*, 217207.

(21) Kim, B. J.; Jin, H.; Moon, S. J.; Kim, J. Y.; Park, B. G.; Leem, C. S.; Yu, J.; Noh, T. W.; Kim, C.; Oh, S. J.; Park, J. H.; Durairaj, J.; Cao, G.; Rotenberg, E. *Phys. Rev. Lett.* **2008**, *101*, 076402.

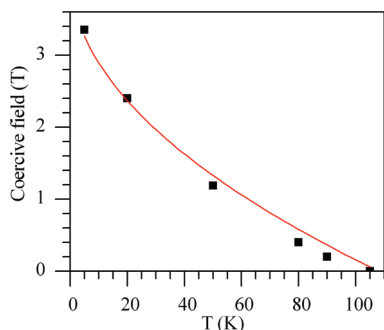


Figure 9. Temperature dependence of the coercive field for CaIrO_3 , showing the fit described in the text.

Rh, Ir, and Pt. These M^{4+} cations are very similar, having a narrow range of ionic radii ($0.60\text{--}0.625\text{ \AA}$)²² and large octahedral crystal field stabilization energies resulting from their low-spin d^n ($n = 4\text{--}6$) electron configurations. A recent density functional theory study²³ of CaRhO_3 suggested that metal–metal bonding in the chains of edge-shared octahedra parallel to the a -axis, as found in the rutile types RuO_2 ,²⁴ IrO_2 ,²⁵ RhO_2 ^{15,16} and ReO_2 ,²⁶ also plays a role. This may account for the ambient pressure stability of postperovskite CaIrO_3 , which has a formal $\text{Ir}^{4+}\text{--Ir}^{4+}$ bond order of 1, in comparison with CaPtO_3 , for which the $\text{Pt}^{4+}\text{--Pt}^{4+}$ bond order is zero. This analysis predicts that CaReO_3 postperovskite (Re^{4+} radius = 0.63 \AA) should also be accessible (but initial syntheses up to 25 GPa and 1400 K have not proved successful). Because the stability conditions for postperovskite oxides are rather severe, it is useful to explore solid solutions between these end-members to increase the range of available materials.

This study has demonstrated that the full series of $\text{CaIr}_{1-x}\text{Pt}_x\text{O}_3$ solid solutions can be stabilized, and the recovery of $\text{CaIr}_{0.5}\text{Rh}_{0.5}\text{O}_3$ suggests that the $\text{CaIr}_{1-x}\text{Rh}_x\text{O}_3$ series should also be accessible. However, the synthesis pressures (~ 15 GPa) required to give near-homogeneous $\text{CaIr}_{1-x}\text{Pt}_x\text{O}_3$ solid solutions were found to be far higher than those to prepare the end-members (1 bar and 4 GPa for $x = 0$ and 1, respectively). Although X-ray diffraction, EDX analysis, and Raman spectroscopy indicate that the

$\text{CaIr}_{1-x}\text{Pt}_x\text{O}_3$ samples are homogeneous, the magnetic measurements show that traces of CaIrO_3 are present.

A pronounced grain growth in the [100] direction is observed for all the samples in this study. This growth gives rise to a large preferred orientation, even in loosely packed powders, and anchoring the particles on a greased surface was required to give XRD data suitable for structure analysis. To the first approximation, no structural change is expected across the $\text{CaIr}_{1-x}\text{Pt}_x\text{O}_3$ series because Ir^{4+} and Pt^{4+} have identical ionic radii of 0.625 \AA . However, some small changes in the lattice parameters and volume are observed experimentally, with evidence for possible local Ir/Pt order from the curvature in the c -parameter variation. The anisotropic connectivity in the postperovskite arrangement creates an intrinsic tendency for the MO_6 octahedra to distort, but the loss of Ir^{4+} spin–orbit effects reduces the distortion of the MO_6 octahedra as x increases in the $\text{CaIr}_{1-x}\text{Pt}_x\text{O}_3$ series.

The electronic ground state of CaIrO_3 appears unconventional because the bulk electronic behavior is semiconducting but the high temperature susceptibility has a temperature-independent variation. This could indicate an intrinsic Pauli paramagnetic and metallic behavior, masked by resistive grain boundaries in the ceramic samples. Alternatively, the ground state may be gapped, with Ir–Ir bonding and spin–orbit coupling effects resulting in a near-zero Ir^{4+} magnetic moment. The small ferromagnetic moment of $0.04\mu_{\text{B}}$ could be consistent with Stoner magnetism in a marginally metallic state or canted order of larger, localized moments. Curie–Weiss paramagnetism emerges as CaIrO_3 is doped with nonmagnetic Pt^{4+} or magnetic Rh^{4+} , which suggests that disruption of a narrow Ir–Ir bonding band may be the dominant effect. The Curie transition is suppressed to zero at $x \approx 0.4$ for Pt doping (assuming a linear $T_{\text{C}}(x)$ variation) but $\text{CaIr}_{0.5}\text{Rh}_{0.5}\text{O}_3$ has $T_{\text{C}} = 40\text{ K}$ showing a clear dependence of the suppression on the magnetic nature of the dopants. The 290 K resistivity of $\text{CaIr}_{0.5}\text{Pt}_{0.5}\text{O}_3$ is 6 orders of magnitude greater than for CaIrO_3 , whereas that of $\text{CaIr}_{0.5}\text{Rh}_{0.5}\text{O}_3$ is almost unchanged, consistent with the loss of hole carriers in the Ir d-band through Pt doping.

Postperovskite CaIrO_3 is also notable for having a very large magnetic anisotropy, comparable to that of hard magnetic materials such as $\text{Nd}_2\text{Fe}_{14}\text{B}$. This demonstrates that permanent magnets could be made from postperovskites containing transition metals with larger spins.

Acknowledgment. We thank EPSRC and the Leverhulme Trust for support.

(22) Shannon, R. D. *Acta Crystallogr.* **1976**, *A32*, 751–767.

(23) Matar, S. F.; Demazeau, G.; Largeteau, A. *Solid State Sci.* **2010**, *12*, 373–378.

(24) Grillo, M. E. *Comput. Mater. Sci.* **2005**, *33*, 83–91.

(25) Shimony, Y.; Ben-dor, L. *J. Mater. Sci. Lett.* **1983**, *2*, 558–560.

(26) Ivanovskii, A. L.; Chupakhina, T. I.; Zubkov, V. G.; Tyutyunnik, A. P.; Krasilnikov, V. N.; Bazuev, G. V.; Okatov, S. V.; Lichtenstein, A. I. *Phys. Lett. A* **2005**, *348*, 66–70.